THE JOURNAL OF PHYSICAL CHEMISTRY C

Article

pubs.acs.org/JPCC

Designed Synthesis of Solid and Hollow $Cu_{2-x}Te$ Nanocrystals with Tunable Near-Infrared Localized Surface Plasmon Resonance

Hong-Jie Yang, Chia-Yu Chen, Fang-Wei Yuan, and Hsing-Yu Tuan*

Department of Chemical Engineering, National Tsing Hua University, 101, Section 2, Kuang-Fu Road, Hsinchu, Taiwan 30013, ROC

Supporting Information

ABSTRACT: Solid and hollow structures of $Cu_{2-x}Te$ nanocrystals are synthesized by the injection of a Te−TOP solution at different reaction times. Both types of $Cu_{2-x}Te$ nanocrystals exhibit an intense absorption peak (localized surface plasmon resonance (LSPR)) in the near-infrared region, arising from excess holes in the valence band, and high molar extinction coefficients of 2.6×10^7 M^{-1} cm^{-1} at 1150 nm and 8.1×10^7 M^{-1} cm^{-1} at 1200 nm are demonstrated for the solid-type and hollow-type $Cu_{2-x}Te$ nanocrystals, respectively. The experimentally observed extinction spectra and calculated extinction spectra based on the electrostatic approximation are studied. The LSPR responses in the near-infrared (NIR) region for both solid and hollow $Cu_{2-x}Te$ nanocrystals are affected by the refractive index of the medium, whereas the NIR resonance shift is more obvious in the hollow-type $Cu_{2-x}Te$ nanocrystals. Furthermore, the localized surface plasmon band of the $Cu_{2-x}Te$ nanostructures can be tuned by post processing via oxidation and reduction methods (controlling their degree of copper deficiency).

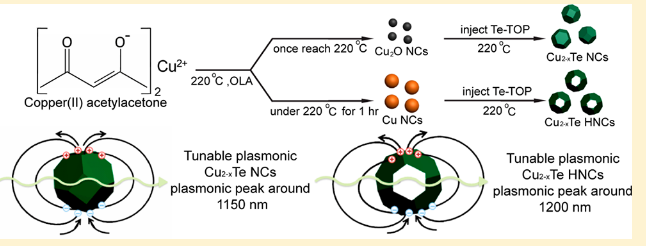

INTRODUCTION

The localized surface plasmon resonance (LSPR) response of colloid nanocrystals has enabled a vast array of applications such as surface-enhanced spectroscopy,[1] biological and chemical sensing,[2] lithographic fabrication,[3] biomedicine,[4] and photovoltaic devices.[5] Metal nanoparticles have been the major materials of interest over the past several decades. However, recent studies found that surface plasmon resonance is not limited to metals but occurs in other materials as well, including conducting metal oxides,[6] transition-metal oxides,[7] and high self-doping semiconductor (copper chalcogenide) nanocrystals.[8−15] These materials also exhibit metallic behavior and a tunable plasmonic response owing to an appreciable free carrier density. For example, Toshiharu et al. demonstrated that the indium tin oxide nanoparticles exhibit surface plasmon resonance in the near-infrared (NIR) region, the position of the NIR absorption band can be tuned by Sn doping to control the surface electron carrier densities or changing the solvent to change the dielectric constant of the surrounding medium.[6] Another example of copper chalcogenide nanoparticles, mainly $Cu_{2-x}S$ and $Cu_{2-x}Se$, with carrier concentrations of $\sim 10^{21}$ cm^{-3} are affected by the Cu-defect density, resulting in LSPR in the NIR region, and have been applied to photothermal therapy.[16,17] These novel plasmonic nanomaterials also exhibit shape-dependent localized surface plasmon resonance which is similar to the metal nanocrystal. For instance, Andrea et al. reported that the anisotropic nanoparticle, $Cu_{2-x}S$ nanodisks, possess two distinct LSPR peaks due to in-plane and out-of-plane dipolar resonances; the LSPR peaks of nanodiscs can be adjusted by changing the diameter and the height of the $Cu_{2-x}S$ nanodisks.[18] Nonetheless, relatively few investigations of closely related materials such as $Cu_{2-x}Te$ nanocrystals have been reported.

Copper telluride is a highly degenerate p-type semiconductor with a band gap that can be tuned by varying the stoichiometry,[19] which has the potential to be applied to photovoltaic devices because its direct band gap (1.18 eV) is suitable for uses as a light absorption layer in solar cell devices.[20] It has been demonstrated that the incorporation of $Cu_{2-x}Te$ in CdTe solar cells improves their NIR transmittance and produces a conductive back contact material for high-efficiency CdTe-based solar cells.[21] In addition, among the copper−chalcogen systems, the binary Cu−Te system is a very complex example.[22] There are different crystal structures depending on relative stoichiometry (e.g., CuTe, Cu_3Te_2, Cu_4Te_3, Cu_7Te_4, and Cu_2Te),[23−27] and in the nonstoichiometric $Cu_{2-x}Te$ cases, several polymorphic transitions occur such that it is difficult to acquire pure products having a single phase.[28] Therefore, only few reports evaluating copper tellurides have been published, including the solvothermal method,[23] hydrothermal method,[29] microwave-assisted synthesis,[30] sonochemical synthesis,[25] and electrochemical synthesis,[31] but the materials produced by the above-mentioned methods normally appear in the form of large or uncontrolled aggregates.

In 2012, several successful methods with high quality for the preparation of copper telluride nanocrystals begin to appear, including copper telluride nanoparticles,[32] nanocubes,[33] hollow

Received: July 30, 2013
Revised: September 22, 2013
Published: September 24, 2013

dx.doi.org/10.1021/jp407559b | J. Phys. Chem. C 2013, 117, 21955−21964

type nanoparticles,[34] nanorods, and tetrapods,[35] wherein the hollow type copper telluride nanocrystals exhibit promising ability to detect carbon monoxide due to the special hollow structure. The $Cu_{2-x}Te$ nanocrystals also display a LSPR peak in the IR region due to copper deficient, which is similar to $Cu_{2-x}S$ and $Cu_{2-x}Se$ nanocrystals.[32]

In the case of metal nanomaterials, it is well-known that the LSPR peaks are significantly affected by the size and shape of metal nanomaterials, as well as surrounding medium.[36] Compared to metal-based nanomaterials, the optical properties of the copper-chalcogenide-based nanoparticles still need future study, but an alternative way to modulate their LSPR peaks is by controlling the copper deficient in their structure. The wavelength of the LSPR peaks can be tuned by varying the degree of copper deficiency via a reduction or oxidation process. For example, a tunable plasmon absorption band can be carried out by reduction (tetrakis(acetonitrile)copper(I) hexafluorophosphate) or oxidation (Ce(IV) ammonium nitrate) of $Cu_{2-x}Se$ nanocrystals to change the copper stoichiometry.[11]

Here, we report the designed colloid synthesis of high-quality plasmonic $Cu_{2-x}Te$ nanocrystals (NCs) and $Cu_{2-x}Te$ hollow nanocrystals (HNCs). These nonstoichiometric $Cu_{2-x}Te$ NCs and $Cu_{2-x}Te$ HNCs show strong surface plasmon resonance with molar excitation compatible with the NIR region because of excess holes in the valence band resulting from copper deficiencies. The NIR plasmonic response of colloidal $Cu_{2-x}Te$ NCs and $Cu_{2-x}Te$ HNCs allowed stepwise tuning by addition of a reducing agent, diisobutylaluminum hydride, which decreased the number of free carriers (decreasing number of copper deficiencies), or oxidation in air, which increased the number of free carriers (i.e., increasing number of copper deficiencies).

■ EXPERIMENTAL SECTION

Chemicals. All chemicals were used as received from the Aldrich, Co., including copper(II) acetylacetonate ($Cu(acac)_2$, 99.99%), elemental Te (99.99%), oleylamine (OLA, 70%), hexane, toluene, ethanol (99.5%), anhydrous toluene, hexane, chloroform, tetrachloroethylene (99%), diisobutylaluminium hydride solution (1 M) in toluene, and trioctylphosphine (TOP, 90%).

Synthesis of $Cu_{2-x}Te$ Nanocrystals. In a reaction of $Cu_{2-x}Te$ NCs, 6 mL of OLA and 0.3 mmol of $Cu(acac)_2$ (0.078 g), in a 50 mL three-neck flask were purged by argon for 30 min. The mixture was then heated to 120 °C for 1 h. Next, the temperature of the mixture was raised to 220 °C. Once the temperature reached 220 °C, 1.5 mL of a 0.1 M TOP−Te solution (stock solution of Te was prepared in an argon-filled glovebox by dissolving 0.025 g of Te in 2 mL of TOP at 150 °C for 1 h) was injected into the reaction flask immediately. The reaction was held at 220 °C for 1 h under argon with continuous stirring. The flask was rapidly cooled to room temperature by a cold water bath. The nanocrystals were isolated by centrifugation at 8000 rpm with addition of 5 mL of toluene and 15 mL of ethanol for 10 min. The washing procedure was repeated twice to remove unreacted precursors and byproducts. The isolated nanocrystals were dispersed in toluene for further characterization.

Synthesis of $Cu_{2-x}Te$ Hollow Nanocrystals. To synthesize $Cu_{2-x}Te$ HNCs, 6 mL of OLA and 0.3 mmol of $Cu(acac)_2$ (0.078 g), in a 50 mL three-neck flask were purged by argon for 30 min. The mixture was then heated to 120 °C for 1 h. Next, the temperature of the mixture was raised to 220 °C and kept at 220 °C for 1h. Thereafter, 1.5 mL of a 0.1 M TOP−Te solution was injected into the reaction flask. The reaction was held at 220 °C for 30 min under argon with continuous stirring. The flask was rapidly cooled to room temperature by a cold water bath. The nanocrystals were isolated by centrifugation at 8000 rpm with addition of 5 mL of toluene and 15 mL of ethanol for 10 min. The washing procedure was repeated twice to remove unreacted precursors and byproducts. The isolated nanocrystals were dispersed in toluene for further characterization.

Characterization. The XRD diffraction pattern was determined on a Rigaku, Ultima IV X-ray diffractometer using Cu Kα radiation operated at 40 kV and 20 mA. TEM, HRTEM, SAED, and EDS were performed on JEOL, JEM 2100F and FEI-TEM, Philips Technai G2 operating at an accelerating voltage of 200 kV equipped with an Oxford INCA EDS, respectively. Samples for TEM imaging were prepared by drop casting the nanocrystals dispersed in toluene onto a 200 mesh carbon-coated copper grid. The XPS measurements were obtained on a a PHI Quantera SXM using a focused monochromatic Al X-ray (1486.6 eV) source at a system pressure of 10^{-9} Torr. The samples for XPS were made by deposition of a nanocrystal suspension in toluene on Si substrates. Electrical transport measurements for $Cu_{2-x}Te$ NCs films were obtained by a Keithley 236 semiconductor parameter analyzer using silver paste to form the contact pads between the probes and the nanocrystal films. UV−vis−NIR absorption spectra were obtained using a Hitachi U-4100 spectrophotometer with the nanocrystals dispersed in tetrachloroethylene or toluene.

Calculations of the Nanocrystal Extinction Spectra. The extinction spectra of the $Cu_{2-x}Te$ NCs and $Cu_{2-x}Te$ HNCs can be theoretically calculated by quasi-static approximation of Mie scattering theory, as described in the following.[13] For spherical particles, the extinction spectrum $\sigma_E(\omega)$ is given by $\sigma_E(\omega) = \sigma_A(\omega) + \sigma_S(\omega)$, where $\sigma_A(\omega)$ is the absorption cross section and $\sigma_S(\omega)$ is the scattering cross section.

$$\sigma_A(\omega) = 4\pi k R^3 Im\left\{\frac{\varepsilon(\omega) - \varepsilon_m}{\varepsilon(\omega) + 2\varepsilon_m}\right\}$$

$$\sigma_S(\omega) = \frac{8}{3}\pi k^4 R^6 \left|\frac{\varepsilon(\omega) - \varepsilon_m}{\varepsilon(\omega) + 2\varepsilon_m}\right|^2$$

In the above equations, k is the wave vector of the incident light, R is the particle radius, ε_m is the dielectric constant of the medium (for tetrachloroethylene, $\varepsilon_m = 2.25$), and $\varepsilon(\omega)$ is the dielectric function of the material. The dielectric function is described by $\varepsilon(\omega) = \varepsilon_1(\omega) + i\varepsilon_2(\omega)$. The $\varepsilon_1(\omega)$ and $\varepsilon_2(\omega)$ are given by:

$$\varepsilon_1(\omega) = \varepsilon_\infty - \frac{{\omega_P}^2}{\omega^2 + \Gamma^2}$$

$$\varepsilon_2(\omega) = \frac{{\omega_P}^2\Gamma}{\omega(\omega^2 + \Gamma^2)}$$

In above equations, ω_P is the bulk plasma frequency of $Cu_{2-x}Te$, Γ is the free carrier damping, ε_∞ is the high-energy dielectric constant of $Cu_{2-x}Te$, and ω is light frequency. The value of ω_P, ε_∞, and Γ were taken from ref 35.

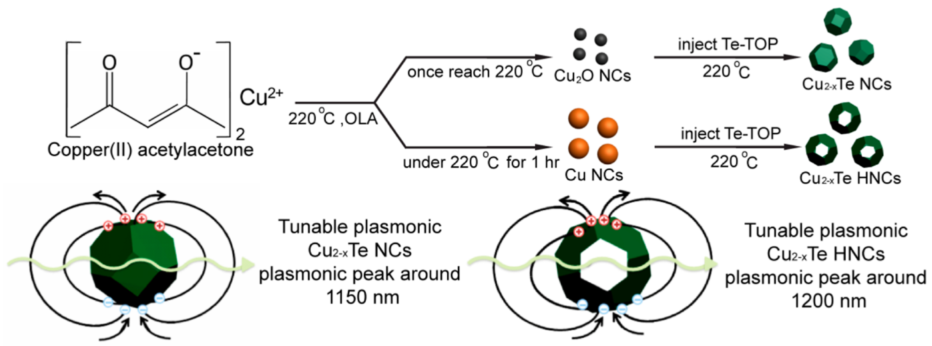

Figure 1. Reaction scheme for the formation of $Cu_{2-x}Te$ NCs and $Cu_{2-x}Te$ HNCs (with surface plasmonic responses) by injecting Te−TOP into a hot $Cu(acac)_2$/OLA solution at different reaction time.

The $Cu_{2-x}Te$ HNCs are treated as core/shell particles. The extinction spectrum, $Q_E(\omega)$, of $Cu_{2-x}Te$ HNCs can be calculated by:[37]

$$Q_E(\omega) = 4xIm \times \left\{ \frac{(\varepsilon_s - \varepsilon_m)(\varepsilon_c + 2\varepsilon_s) + (1-g)(\varepsilon_c - \varepsilon_s)(\varepsilon_m + 2\varepsilon_s)}{(\varepsilon_s + 2\varepsilon_m)(\varepsilon_c + 2\varepsilon_s) + (1-g)(2\varepsilon_s - 2\varepsilon_m)(\varepsilon_c - \varepsilon_s)} \right\}$$

where ε_s is the dielectric function of the shell layer, ε_c is the dielectric constant of the core, and ε_m is the dielectric constant of the medium (in our system, $\varepsilon_c = \varepsilon_m = 2.25$). The volume fraction of the shell layer, g, and the size parameter, x, are given by:

$$x = \frac{2\pi R_o {\varepsilon_m}^{1/2}}{\lambda}$$

$$g = \frac{{R_o}^3 - {R_i}^3}{{R_o}^3}$$

where R_o is the outer radius of $Cu_{2-x}Te$ HNCs, λ is the wavelength of light, and R_i is the inner radius of $Cu_{2-x}Te$ HNCs.

Reduction Process of the $Cu_{2-x}Te$ Nanocrystals and $Cu_{2-x}Te$ Hollow Nanocrystals. The reduction process was carried out under argon atmosphere. First, a spectrum of absorption was measured by dispersing the nanocrystals in anhydrous toluene (0.12 mg/mL) in a 1 cm airtight screw cap quartz cuvette cell. Subsequently, 10 μL of reduction agent (diisobutylaluminium hydride solution 0.1 M in toluene) was added into the nanocrystal solution, and the absorption spectra were recorded immediately afterward. For both types of $Cu_{2-x}Te$ NCs, the reduction process usually needed to be repeated three times to fully eliminate the LSP band in the NIR region.

Oxidation Process of the $Cu_{2-x}Te$ Nanocrystals and $Cu_{2-x}Te$ Hollow Nanocrystals. The oxidation process was carried out under ambient atmosphere. The screw cap of the same batch of nanocrystal solution after full reduction was removed, and oxidization was performed under ambient atmosphere. The absorption spectra of the nanocrystal solution were recorded with time during the oxidation process. For the solid and hollow type $Cu_{2-x}Te$ nanocrystals, 3 h and less than 1 h, respectively, are required to fully recover the LSP band.

Calculation of the Molar Extinction Coefficient. The molar extinction coefficient of $Cu_{2-x}Te$ NCs and $Cu_{2-x}Te$ HNCs were calculated from the Beer−Lambert law by measuring the experimental absorbances for various concentrations of nanocrystals in trichloroethylene.

$$A(\lambda) = \epsilon(\lambda)LC$$

In the above equations, A is the absorbance at specific wavelength λ, ϵ is the molar extinction coefficient, L is the path length of the cuvette (1 cm), and C is the concentration of nanocrystals in solution (mole L^{-1}). The mass contribution (X) from surface ligands was measured by thermogravimetric analysis (TGA, Figure S8).

$$C_{wt,m} = C_{wt} \times (1 - X)$$

C_{wt} is the weight concentration of the nanocrystals with surface ligands (g L^{-1}) and $C_{wt,m}$ is the true weight concentration of the nanocrystals (g L^{-1}). The concentration (L $mole^{-1}$) of nanocrystals is calculated using the following:

$$C = \frac{C_{wt,m}}{M_{NC}} = C_{wt}(1 - X)/\left(\frac{4}{3}\pi R^3 \rho_{Cu_{2-x}Te} N_A\right)$$

M_{NC} is the molar weight of the nanocrystals (g mol^{-1}), N_A is Avogadro's constant (mol^{-1}), R is the average radius of the nanocrystals, assuming the nanocrystals are spherical (for the case of $Cu_{2-x}Te$ HNCs, $R^3 = {R_o}^3 - {R_i}^3$, where R_o is the average outer radius, R_i is the average inner radius). On the basis of the TEM and XRD results, we assume that the radius for $Cu_{2-x}Te$ NCs is 4.4 nm. For the equation, ρ (g cm^{-3}) is the density of the $Cu_{2-x}Te$ NCs (7.27 g cm^{-3}). Figure 4 shows the absorbance spectrum of the $Cu_{2-x}Te$ NCs and $Cu_{2-x}Te$ HNCs with different nanocrystal concentrations and linear fits of Beer−Lambert Law to the absorbance at various wavelengths. Using the true $Cu_{2-x}Te$ mass, the molar extinction coefficient is calculated by:

$$\epsilon(\lambda)(M^{-1}cm^{-1}) = \frac{A(\lambda)}{LC} = \frac{A(\lambda)\frac{4}{3}\pi R^3 \rho_{Cu_{2-x}Te} N_A}{LC_{wt}(1 - X)}$$

Determination of the Optical Band Gap. The direct optical band gap E_g of copper telluride can be determined with the relation.

$$B(h\nu - Eg) = \alpha h\nu^n$$

Where α is the absorption coefficient, $h\nu$ is the incident photon energy, n is 2 for a direct transition, E_g is the optical band gap and B is a constant. The experimental values of $(\alpha h\nu)^2$ against $h\nu$ are plotted in Figure 7a.

dx.doi.org/10.1021/jp407559b | J. Phys. Chem. C 2013, 117, 21955−21964

■ RESULTS AND DISCUSSION

The $Cu_{2-x}Te$ NCs and $Cu_{2-x}Te$ HNCs were synthesized by injecting a Te−TOP solution into a hot $Cu(acac)_2$/OLA solution at different injection times, as shown in Figure 1. To form $Cu_{2-x}Te$ NCs, the Te−TOP solution was injected into the $Cu(acac)_2$/OLA solution heated to 220 °C. At the beginning of the synthesis, small nanocrystals with an average diameter of approximately 4 nm appear before the injection of Te−TOP. The XRD pattern and UV−vis−NIR absorbance spectra of these small nanoparticles (Figure S1) confirm that they are Cu_2O NCs. Following rapid injection of Te−TOP at this time, copper oxide transforms to $Cu_{2-x}Te$ NCs while the solution rapidly transforms from black to dark green.

Figure 2a shows a TEM image of $Cu_{2-x}Te$ NCs having good monodispersity with an average diameter of 8.8 nm and the standard deviation of 1.8 nm, which is in agreement with the value obtained from X-ray diffraction (Figure 2d). A detailed crystal structure of the $Cu_{2-x}Te$ NCs was determined by selected-area electron diffraction (Figure S2a) and is consistent with the hexagonal phase of $Cu_{2-x}Te$. HRTEM (Figure 2b and Figure S3) and its fast Fourier transform (Figure 2c) provide more detailed structural information for the individual nanoparticles with distinct lattice fringe patterns, indicating the high crystallinity of the nanocrystals. It can be observed that the interfringe distance of 0.36 nm corresponds to the (200) planes of the hexagonal $Cu_{2-x}Te$ form. XRD (Figure 2d) of the $Cu_{2-x}Te$ NCs confirms that they were formed after the injection of Te−TOP. No other phases, such as Cu, CuO, Cu_2O, or Te, and other stoichiometric crystalline phases, such as CuTe, Cu_3T_2, or Cu_7Te_4, were found.

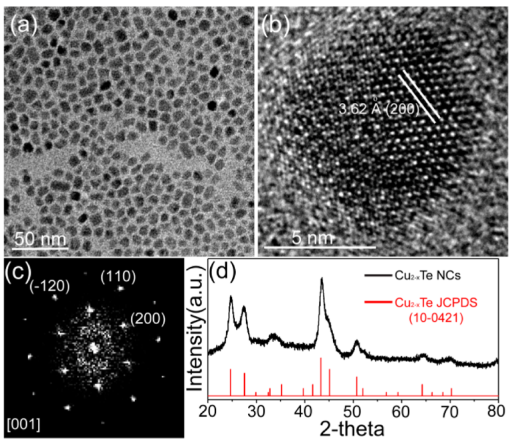

Figure 2. (a) TEM image of $Cu_{2-x}Te$ NCs. (b) HRTEM image of a single $Cu_{2-x}Te$ NC and (c) its fast Fourier transform. (d) XRD pattern of $Cu_{2-x}Te$ NCs.

The $Cu_{2-x}Te$ HNCs were generated by the injection of Te−TOP into the $Cu(acac)_2$/OLA solution heated at 220 °C for 1 h, as shown in Figure 1. The Cu NCs had already formed before the injection of Te−TOP (Figure S4 shows the TEM images of the Cu NCs as well as their XRD pattern and UV−vis−NIR absorbance spectra). After the injection of the Te−TOP solution, $Cu_{2-x}Te$ HNCs were formed. Concurrently, the color of the solution turned from dark red to dark green. Figure 3a shows a TEM image of the $Cu_{2-x}Te$ HNCs, whereby the center of the $Cu_{2-x}Te$ HNCs appears brighter after telluride addition, indicating that most of the nanocrystals have voids inside them. Some voids are not located at the center of the $Cu_{2-x}Te$ HNCs, and some shells appear to be partially fractured. These $Cu_{2-x}Te$ HNCs possess irregular surface shapes. The SAED pattern of the $Cu_{2-x}Te$ HNCs (Figure S2b) is also consistent with the hexagonal phase of $Cu_{2-x}Te$, and TEM image shows that the average outer diameter of the $Cu_{2-x}Te$ HNCs is 16.5 nm with a standard deviation of 2.7 nm. HRTEM (Figure 3b and Figure S5) and its fast Fourier transform (Figure 3c) show that the lattices of the $Cu_{2-x}Te$ HNCs in the shell are arranged in different directions and also confirm that the shells of the $Cu_{2-x}Te$ HNCs are multicrystalline. Figure 3d shows an XRD pattern of the $Cu_{2-x}Te$ HNCs. It can be observed that all reflection peaks are consistent with those of a hexagonal structure [space group ($P3m1$) (156)] with lattice constants $a = 8.342$ Å and $c = 21.69$ Å, which are in good agreement with the published data for $Cu_{2-x}Te$ (JCPDS file no. 10-0421 for $Cu_{2-x}Te$). The XRD pattern, in which no other diffraction peaks are observed, indicates the purity of the $Cu_{2-x}Te$ HNCs. We have collected additional products at different reaction times after the injection of Te−TOP to observe intermediate states. The Cu core disappears in 15 s after the injection of Te−TOP, and only very few filament-like bridges connecting the Cu core inside the crystals and the telluride shell were observed (Figure S6, black arrow), the phenomenon has been observed in many cases.[38,39] The filament-like bridges in the crystals are nearly absent in 1 min after the injection of Te−TOP. Thus, the formation of the $Cu_{2-x}Te$ HNCs was complete by this time, and further prolonging the reaction would not afford any changes in the amount of products. With respect to the $Cu_{2-x}Te$ HNCs growth development, initially, thin layers of $Cu_{2-x}Te$ grow onto the Cu core surface, and then the nanoscale Kirkendall process occurs at the interface between the Cu core and telluride shell. Overall, it took approximately 1 min to completely convert Cu NCs into $Cu_{2-x}Te$ HNCs. If Te transport (inward) is negligible compared with Cu transport (outward) through the telluride shell, the final hole size of the $Cu_{2-x}Te$ HNCs will closely match that of the original Cu NCs. However, we found that the outer diameter of the $Cu_{2-x}Te$ HNCs (16.5 nm) is greater than that of the initial Cu NCs (13.5 nm), indicating that the volume of the $Cu_{2-x}Te$ HNCs is approximately 1.8 times greater than

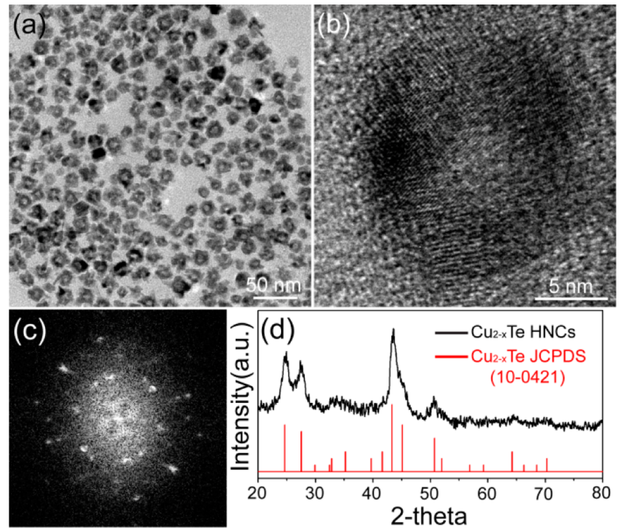

Figure 3. (a) TEM image of $Cu_{2-x}Te$ HNCs. (b) HRTEM image of a single $Cu_{2-x}Te$ HNC and (c) its fast Fourier transform. (d) XRD pattern of $Cu_{2-x}Te$ HNCs.

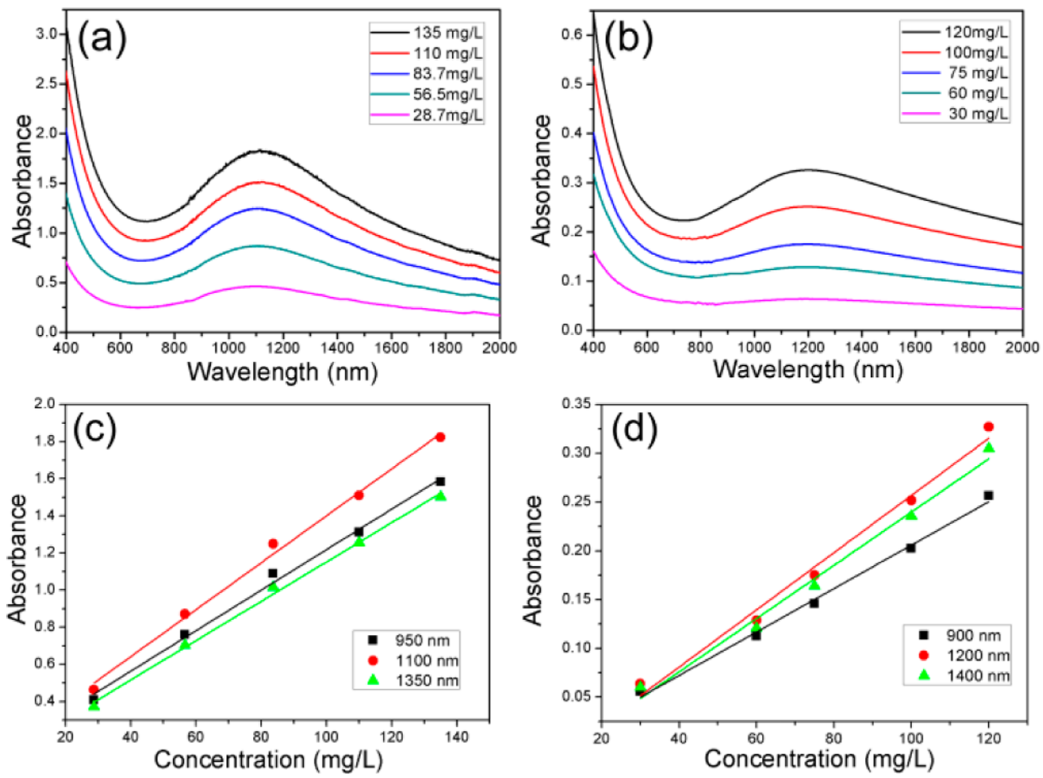

Figure 4. UV−vis−NIR absorbance spectra of (a) $Cu_{2-x}Te$ NCs and (b) $Cu_{2-x}Te$ HNCs measured at different concentration of nanocrystals in trichloroethylene. Plots of absorbance vs concentration for (c) $Cu_{2-x}Te$ NCs and (d) $Cu_{2-x}Te$ HNCs at specific wavelength with linear regression curve.

that of the initial Cu NCs. Furthermore, the average inner diameter (5.9 nm) of the $Cu_{2-x}Te$ HNCs is smaller than the diameter of the initial Cu NCs. This indicates significant inward diffusion of Te atoms or inward deformation of the shell during the growth process. Some broken shells were clearly observed (Figure S6, red arrow). We speculate that this is caused by significant inward deformation or phase changes (lattice-mismatch-induced stress).[40,41] These broken shells created some gaps allowing material exchange between the core Cu NCs and liquid Te−TOP through the gaps, further accelerating the hollowing process. EDS (Figure S7) of the $Cu_{2-x}Te$ NCs and $Cu_{2-x}Te$ HNCs shows the presence of Cu and Te with an average atomic ratio of (Cu/Te) approximately 2. This is in contrast to LSPR in the NIR region that results from the formation of vacancies in the Cu lattice, indicating that the x value of $Cu_{2-x}Te$ should be greater than 0. We will discuss this point below.

By estimating the molar NC concentration (C) and measuring the experimental absorbance (Figure 4), one can obtain a good estimate of the extinction coefficient $\epsilon(\lambda)$ for these NCs. Figure 5a,b shows typical room temperature UV−vis−NIR optical absorption spectra and extinction coefficient $\epsilon(\lambda)$ from the measured absorbance of $Cu_{2-x}Te$ NCs and $Cu_{2-x}Te$ HNCs dispersed in trichloroethylene. For both $Cu_{2-x}Te$ NCs and $Cu_{2-x}Te$ HNCs, air exposure does not induce further spectral changes. Two obvious absorption peaks are observed. The first is a shoulder observed at wavelengths below 650 nm, which can be attributed to the direct band absorption.[42−44] The second is a broad and intense absorption peak centered at 1150 nm for the $Cu_{2-x}Te$ NCs and 1200 nm for the $Cu_{2-x}Te$ HNCs, respectively. The NIR absorption band from copper chalcogenides was assigned to surface plasmon resonance rather than to an indirect interband transition.[8,10,11,32,44] For indirect band gap semiconductors, the electronic transition from the valence band to the conduction band is phonon assisted, and the momentum and energy of the electron−hole pair are changed in the band-to-band transition. Therefore, their absorption and emission are weak. For plasmonic nanomaterials, the LSPR is a collective oscillation of surface free carriers within the $Cu_{2-x}Te$ NCs induced by interaction with light so as to enhance light absorption and scattering near the resonance frequency. The obtained molar extinction coefficients of $\sim 10^7$ M^{-1} cm^{-1} for the $Cu_{2-x}Te$ NCs and $Cu_{2-x}Te$ HNCs (2.6×10^7 M^{-1} cm^{-1} at 1150 nm for $Cu_{2-x}Te$ NCs and 8.1×10^7 M^{-1} cm^{-1} at 1200 nm for $Cu_{2-x}Te$ HNCs) are consistent with plasmon absorption and are several orders of magnitude higher than those of strong organic sensitizers[45] and semiconductor quantum dots (lead chalcogenides)[46,47] but lower than those of metal nanocrystals.[48,49] As indicated in Figure 5c, there is a slight difference in the NIR response between the solid and hollow $Cu_{2-x}Te$ nanocrystals. It is well-known that LSPR is strongly dependent on nanoparticle size and shape.[36] For example, hollow gold nanocrystals exhibit surface plasmon bands that are tunable by controlling nanocrystal size and shell thickness.[50] Therefore, in our case, the difference in the position of the surface plasmon band will also be affected by nanocrystal size and shape. According to many examples of metal shell-based calculation,[51,52] near-field enhancements within the shell were observed. The effect of local-field enhancement increases with increasing the radius of the shell when the shell layers are thick enough. In the case of $Cu_{2-x}Te$ HNCs, there is some degree of field enhancement inside the $Cu_{2-x}Te$ HNCs and some portion of the enhancement coming from surface roughness. In addition,

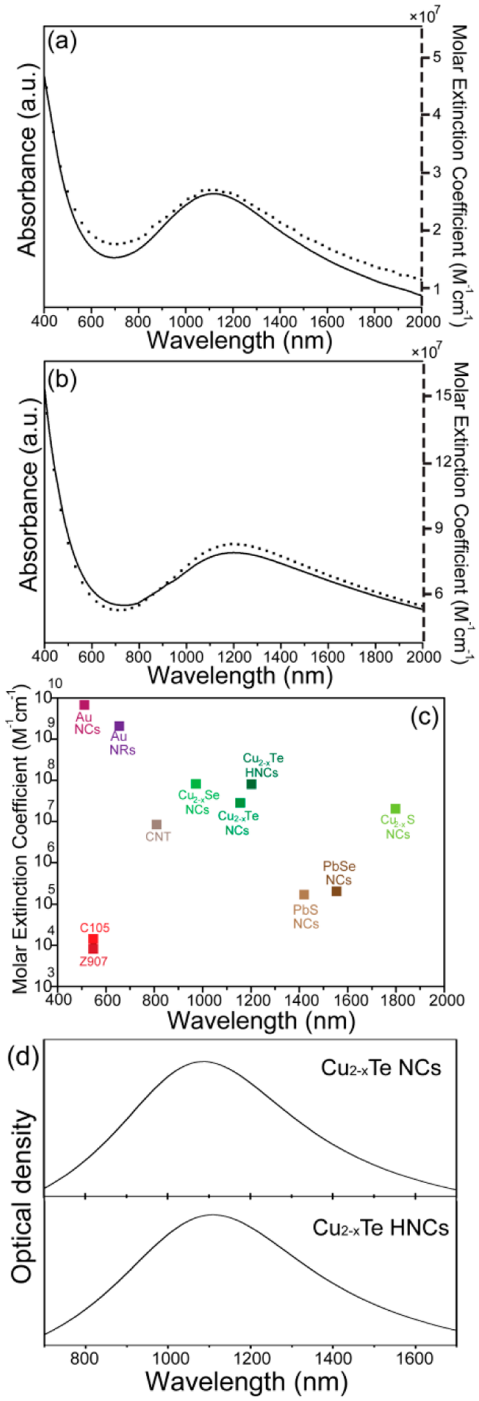

Figure 5. Absorbance (dotted line) and molar extinction coefficient (solid line) for (a) $Cu_{2-x}Te$ NCs and (b) $Cu_{2-x}Te$ HNCs. (c) Molar extinction coefficients of an organic sensitizer (C105 and Z907[44]), carbon nanotubes,[58] gold nanostructures (nanoparticles[48] and nanorods[49]), lead chalcogenide (PbS[46] and PbSe[47]), and copper chalcogenide ($Cu_{2-x}S$[10] and $Cu_{2-x}Se$[17]) nanocrystals at a specific wavelength. (d) Calculated extinction spectra of $Cu_{2-x}Te$ NCs and $Cu_{2-x}Te$ HNCs.

TEM results indicate that the shell is polycrystalline (not a perfect shell); therefore, many pinholes (only few nm) may exist on the surface, resulting in electromagnetic field enhancement provided by the hot spots (pinhole), just like the metal nanoshells cases.[52]

To further understand the effect of the nanocrystal morphology on the plasmonic properties, we calculated their extinction spectra using the electrostatic approximation. Figure 5d shows calculated extinction spectra of $Cu_{2-x}Te$ NCs and $Cu_{2-x}Te$ HNCs, which both exhibit a similar plasmon band located in the NIR region. For $Cu_{2-x}Te$ NCs and $Cu_{2-x}Te$ HNCs, peaks are located at 1090 nm (1150 nm for the experiment) and 1110 nm (1200 nm for the experiment), respectively. There are two possible reasons for the disparity between experimental and calculated extinction spectra, the size and shape deviation and the surface state of $Cu_{2-x}Te$ NCs. In addition, the polycrystalline nature (concentration of grain boundaries and defects) of the $Cu_{2-x}Te$ HNCs should also play an important role in plasmon response.[53] Based on experimental and calculated extinction spectra, the plasmon band of $Cu_{2-x}Te$ HNCs would red shift relative to the $Cu_{2-x}Te$ NCs either in the experimental or calculated extinction spectra. In the case of $Cu_{2-x}Te$ HNCs, the inside and outside surface charges generated by the incident electric field should interact with each other to generate the plasmon response. Therefore, the plasmon response of $Cu_{2-x}Te$ HNCs should be sensitive to the inner and outer diameter. This phenomenon is similar to that occurring in the metal nanoshell, which has a red shift in the absorption band as the solid metal nanoparticles become hollow type.[50]

Hall effect measurements confirmed the p-type conductivity of the $Cu_{2-x}Te$ NCs, and the carrier concentration for the sample at room temperature was determined to be 1.25×10^{21} cm^{-3}. The large number of free carriers (holes) confirms the degenerate (self-doping) semiconducting behavior of $Cu_{2-x}Te$ (free carrier concentration $>10^{17}$ cm^{-3}) and explains the large photon absorption in the NIR region, which reasonably agrees with previously reported ones.[18,19] Hole densities of 10^{21} cm^{-3} are typical in copper chalcogenide films and strongly depend on the method of preparation of the specimens, and consequently on the value of x, and vary from 10^{18} to 10^{21} cm^{-3}.

The plasmonic response of $Cu_{2-x}Te$ NCs and $Cu_{2-x}Te$ HNCs can be varied by post processing control of the composition. We added small amounts of a reducing agent, 0.1 M diisobutylaluminum hydride in toluene, stepwise to $Cu_{2-x}Te$ NC and $Cu_{2-x}Te$ HNC solutions. As a result, the LSP band of the $Cu_{2-x}Te$ NCs and $Cu_{2-x}Te$ HNCs ($x > 0$, red curve in Figure 6a,c) significantly red shifts and decreases in intensity until it nearly vanishes ($x \approx 0$, black curve in Figure 6a,c), and the interband region transition also red shifts, but the intensity increases. In addition, we plotted $(\alpha h\nu)^2$ against hν (Figure 7a); it shows that the direct band gap of $Cu_{2-x}Te$ NCs decreases with x, which is consistent with the $Cu_{2-x}Te$ thin film results.[54] On the basis of the XPS analysis (Figure S9), we suggest that the surface of the $Cu_{2-x}Te$ NCs and $Cu_{2-x}Te$ HNCs has some Cu^{2+} species from the a thin layer of CuO or Cu(II) atoms bound to surface ligands. A similar formation was also observed for Cu_2Se NCs[55] and $Cu_{2-x}Te$ NCs.[32] Thus, the EDS analysis of Cu/Te is often equal to 2. We suggest that adding the reducing agent may drive the reduction of Cu^{2+} to Cu^+, so Cu^+ can be reinserted into the lattices from the surface layer (Te atoms form regular lattices, whereas copper atoms are statistically distributed in disorder, occupying the interstices of the Te lattice, which makes Cu mobile),[56] thus reducing copper vacancies (i.e., reduction of the number of free carriers) and decreasing the direct band gap of $Cu_{2-x}Te$ NCs. Therefore, a gradual red shift and decrease in the intensity of the NIR LSP band occurs. After the same samples of $Cu_{2-x}Te$ NCs and

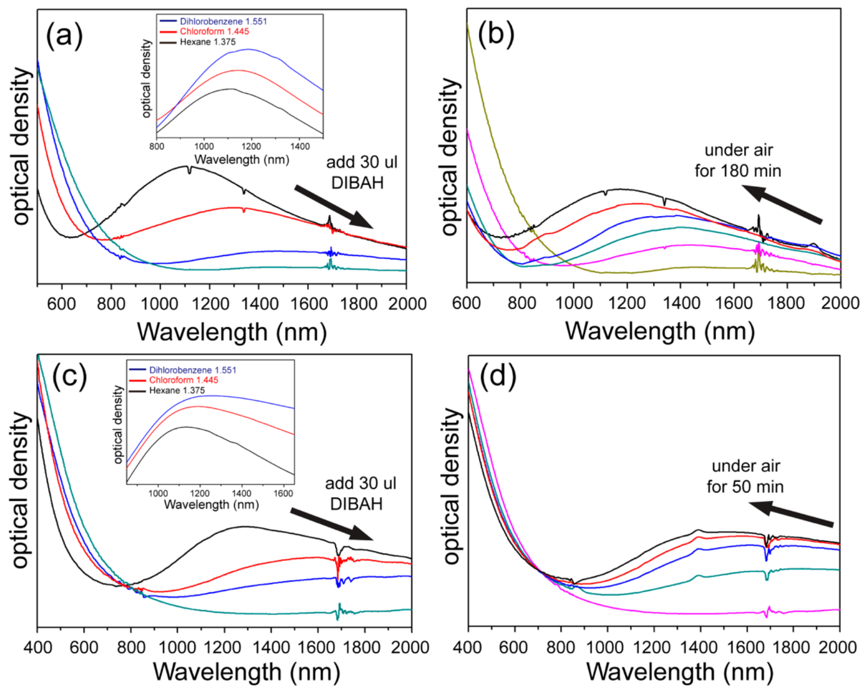

Figure 6. Evolution of the absorbance spectra of (a) $Cu_{2-x}Te$ NCs and (c) $Cu_{2-x}Te$ HNCs in toluene treated by stepwise addition of different amounts of a reducing agent. Time evolution of the absorbance spectra of (b) $Cu_{2-x}Te$ NCs and (d) $Cu_{2-x}Te$ HNCs during oxidation by exposure to air. Insets of (a) and (c) show the absorbance spectra of $Cu_{2-x}Te$ NCs and $Cu_{2-x}Te$ HNCs dispersed in hexane, chloroform, and dichlorobenzene with refractive indices of 1.375, 1.455, and 1.551, respectively.

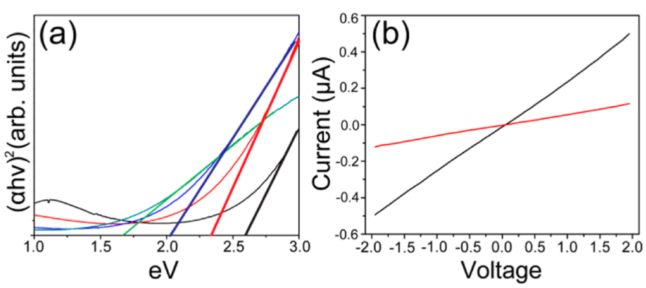

Figure 7. Plots $(\alpha h\nu)^2$ vs $h\nu$ for the $Cu_{2-x}Te$ NCs after synthesis and addition of various amounts of the reducing agent. (b) Current−voltage measurements of thin films of $Cu_{2-x}Te$ NCs before (black line) and after (red line) reduction procedure.

$Cu_{2-x}Te$ HNCs were oxidized under air, respectively, for 3 h and 50 min, emergence of an optical response in NIR and then a gradual blue shift and spectral narrowing are observed. On the other hand, the interband transition region also undergoes a gradual blue shift, as shown in Figure 6b,d. The time required for oxidation of $Cu_{2-x}Te$ HNCs was significantly less than that required for $Cu_{2-x}Te$ NCs. While the oxidation rate depends on many parameters, we presume that the major difference in our case is associated with the surface area because the inner surface of $Cu_{2-x}Te$ HNCs can potentially contribute to the oxidation rate owing to its internal void core and open hollow structure (the small O_2 molecule could penetrate the polycrystalline shell through the grain boundaries). As the oxidation proceeds, exposure to air drives the oxidation of Cu^+ to Cu^{2+}, thereby increasing copper vacancies in the $Cu_{2-x}Te$ NCs (increase in the number of free carriers). Consequently, the NIR band regains intensity and gradually blue shifts during oxidation. XRD, TEM, and SAED analyses confirm that before and after reduction (Figure 8), the crystal structure and morphology of the $Cu_{2-x}Te$ NCs were the same. LSPR is also sensitive to the refractive index of the surrounding medium.[57] We compared the NIR spectra of the $Cu_{2-x}Te$ NCs (Figure 6a inset) and $Cu_{2-x}Te$ HNCs (Figure 6c inset) in anhydrous hexane, anhydrous chloroform, and anhydrous 1,2-dichlorobenzene (refractive indices of 1.375, 1.445, and 1.551, respectively). For both solid and hollow types of $Cu_{2-x}Te$ NCs, the LSPR peaks are red shifted with increasing refractive index of the medium, which is in agreement with the LSPR behavior. This provides an additional way to adjust the NIR LSPR band of $Cu_{2-x}Te$ NCs by changing the refractive index of the medium. In addition, the LSPR resonances of hollow type (hexane: 1134 nm. chloroform: 1190 nm. 1,2-dichlorobenzene: 1257 nm.), have larger red shifts than the solid type (hexane: 1114 nm. chloroform: 1143 nm. 1,2-dichlorobenzene: 1186 nm). This phenomenon can be explained because the $Cu_{2-x}Te$ HNCs offer more exposed surface area to solvents than the solid type in the experiments.

Furthermore, we also measured the conductive properties of $Cu_{2-x}Te$ NC films, which were prepared by drop casting a nanocrystalline colloidal solution onto glass substrates before and after reduction. The average film thickness was 25 μm. Then, a silver electrode was patterned using a silver paste. The gap and length of the two electrodes were both 5 mm. The current−voltage (I−V) measurements were taken by employing a two-probe method using a Keithley 236 Source Meter. As shown in Figure 7b, the films of the $Cu_{2-x}Te$ NCs were recorded immediately before and after the reduction process. We found that the film resistivities of the $Cu_{2-x}Te$ NCs before and after the completed reduction were 1.78 and 11.78 Ω cm, respectively, and were dependent on the stoichiometry (x); as x decreases, ρ increases, which is consistent with the $Cu_{2-x}Te$ thin film.[19]

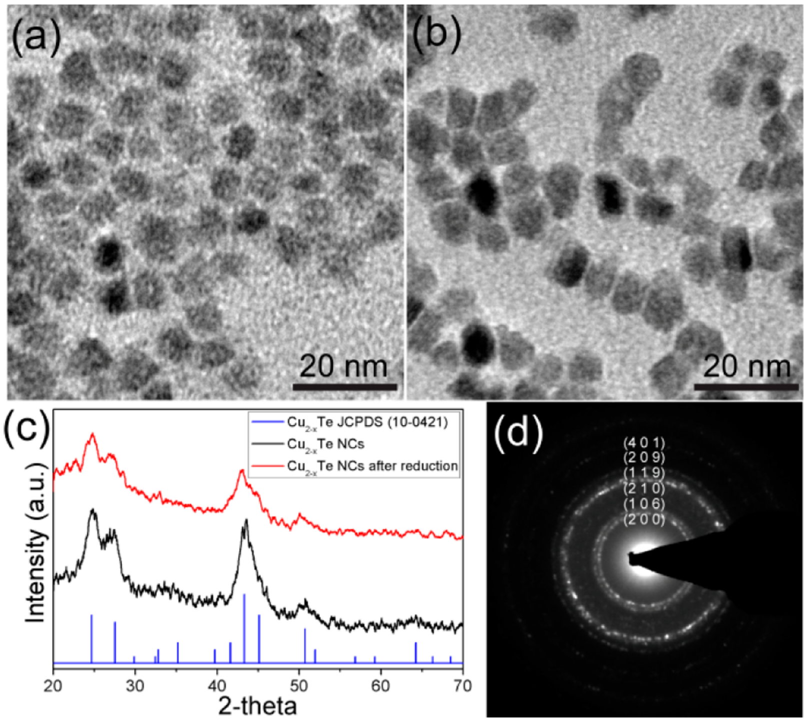

Figure 8. TEM images of $Cu_{2-x}Te$ NCs before (a) and after (b) reduction procedure. (c) XRD pattern of $Cu_{2-x}Te$ NCs before and after reduction procedure. (d) SAED pattern of $Cu_{2-x}Te$ NCs after reduction procedure.

■ CONCLUSIONS

In conclusion, high-quality $Cu_{2-x}Te$ NCs and $Cu_{2-x}Te$ HNCs were prepared using Cu(acac)2 in OLA and Te in TOP as the precursors at 220 °C. $Cu_{2-x}Te$ HNCs were formed by implementing the nanoscale Kirkendall effect, in which Cu nanoparticles were formed first followed by the injection of Te−TOP solution. The optical absorption spectra of $Cu_{2-x}Te$ NCs and $Cu_{2-x}Te$ HNCs show two obvious absorption peaks; the low wavelength absorbance is due to interband transition, and NIR absorptions are due to surface plasmon resonance. Further, the NIR plasmonic responses of colloidal $Cu_{2-x}Te$ NCs can be reversibly tuned by stepwise addition of a reducing agent or oxidation in air and fine-tuned by changing the refractive index of the medium. In addition, the hollow type $Cu_{2-x}Te$ NCs is more sensitive to the surrounding medium than the solid type. This is an effective method for adjusting the optical properties of optoelectronic devices and materials used in biomedical applications that require NIR absorption.

■ ASSOCIATED CONTENT

Supporting Information

TEM, XRD, absorbance spectra of Cu_2O and Cu nanocrystals; TEM, SAED, EDS, TGA, and XPS information of solid and hollow $Cu_{2-x}Te$ nanocrystals. This material is available free of charge via the Internet at http://pubs.acs.org.

■ AUTHOR INFORMATION

Corresponding Author

*E-mail: hytuan@che.nthu.edu.tw. Fax: + 886-3-571-5408. Tel.: + 886-3-572-3661

Notes

The authors declare no competing financial interest.

■ ACKNOWLEDGMENTS

The authors acknowledge the financial support by the National Science Council of Taiwan (NSC 102-2221-E-007-023-MY3 and NSC 101-2623-E-007-013-IT), the Minitry of Economic Affairs, Taiwan (101-EC-17-A-09-S1-198), and the National Tsing Hua University (102N2051E1, 102N2061E1). Assistance with HRTEM (JEOL JEM-2100F) was provided by the Tamkang University College of Science and by the Center for Energy and Environmental Research, National Tsing Hua University.

■ REFERENCES

(1) Golab, J. T.; Sprague, J. R.; Carron, K. T.; Schatz, G. C.; Vanduyne, R. P. A Surface Enhanced Hyper-Raman Scattering Study of Pyridine Adsorbed onto Silver—Experiment and Theory. *J. Chem. Phys.* **1988**, *88*, 7942−7951.
(2) Endo, T.; Yamamura, S.; Nagatani, N.; Morita, Y.; Takamura, Y.; Tamiya, E. Localized Surface Plasmon Resonance Based Optical Biosensor Using Surface Modified Nanoparticle Layer for Label-Free Monitoring of Antigen-Antibody Reaction. *Sci. Technol. Adv. Mater.* **2005**, *6*, 491−500.
(3) Srituravanich, W.; Fang, N.; Sun, C.; Luo, Q.; Zhang, X. Plasmonic Nanolithography. *Nano Lett.* **2004**, *4*, 1085−1088.
(4) Loo, C.; Lowery, A.; Halas, N. J.; West, J.; Drezek, R. Immunotargeted Nanoshells for Integrated Cancer Imaging and Therapy. *Nano Lett.* **2005**, *5*, 709−711.
(5) Atwater, H. A.; Polman, A. Plasmonics for Improved Photovoltaic Devices. *Nat. Mater.* **2010**, *9*, 865−865.
(6) Kanehara, M.; Koike, H.; Yoshinaga, T.; Teranishi, T. Indium Tin Oxide Nanoparticles with Compositionally Tunable Surface Plasmon Resonance Frequencies in the Near-IR Region. *J. Am. Chem. Soc.* **2009**, *131*, 17736−17737.
(7) Manthiram, K.; Alivisatos, A. P. Tunable Localized Surface Plasmon Resonances in Tungsten Oxide Nanocrystals. *J. Am. Chem. Soc.* **2012**, *134*, 3995−3998.

(8) Luther, J. M.; Jain, P. K.; Ewers, T.; Alivisatos, A. P. Localized Surface Plasmon Resonances Arising from Free Carriers in Doped Quantum Dots. *Nat. Mater.* **2011**, *10*, 361−366.
(9) Scotognella, F.; Della Valle, G.; Kandada, A. R. S.; Dorfs, D.; Zavelani-Rossi, M.; Conforti, M.; Miszta, K.; Comin, A.; Korobcheyskaya, K.; Lanzani, G.; et al. Plasmon Dynamics in Colloidal $Cu_{2-x}Se$ Nanocrystals. *Nano Lett.* **2011**, *11*, 4711−4717.
(10) Zhao, Y. X.; Pan, H. C.; Lou, Y. B.; Qiu, X. F.; Zhu, J. J.; Burda, C. Plasmonic $Cu_{2-x}S$ Nanocrystals: Optical and Structural Properties of Copper-Deficient Copper(I) Sulfides. *J. Am. Chem. Soc.* **2009**, *131*, 4253−4261.
(11) Dorfs, D.; Hartling, T.; Miszta, K.; Bigall, N. C.; Kim, M. R.; Genovese, A.; Falqui, A.; Povia, M.; Manna, L. Reversible Tunability of the Near-Infrared Valence Band Plasmon Resonance in $Cu_{2-x}Se$ Nanocrystals. *J. Am. Chem. Soc.* **2011**, *133*, 11175−11180.
(12) Xie, Y.; Carbone, L.; Nobile, C.; Grillo, V.; D'Agostino, S.; Della Sala, F.; Giannini, C.; Altamura, D.; Oelsner, C.; Kryschi, C.; et al. Metallic-like Stoichiometric Copper Sulfide Nanocrystals: Phase- and Shape-Selective Synthesis, Near-Infrared Surface Plasmon Resonance Properties, and Their Modeling. *ACS Nano* **2013**, *7*, 7352−7369.
(13) Scotognella, F.; Valle, G.; Srimath Kandada, A.; Zavelani-Rossi, M.; Longhi, S.; Lanzani, D.; Tassone, F. Plasmonics in Heavily-Doped Semiconductor Nanocrystals. *Eur. Phys. J. B* **2013**, *86*, 1−13.
(14) Liu, X.; Wang, X.; Zhou, B.; Law, W.-C.; Cartwright, A. N.; Swihart, M. T. Size-Controlled Synthesis of $Cu_{2-x}E$ (E = S, Se) Nanocrystals with Strong Tunable Near-Infrared Localized Surface Plasmon Resonance and High Conductivity in Thin Films. *Adv. Funct. Mater.* **2013**, *23*, 1256−1264.
(15) Li, W.; Zamani, R.; Rivera Gil, P.; Pelaz, B.; Ibáñez, M.; Cadavid, D.; Shavel, A.; Alvarez-Puebla, R. A.; Parak, W. J.; Arbiol, J.; et al. CuTe Nanocrystals: Shape and Size Control, Plasmonic Properties and Use as SERS Probes and Photothermal Agents. *J. Am. Chem. Soc.* **2013**, *135*, 7098−7101.
(16) Li, Y. B.; Lu, W.; Huang, Q. A.; Huang, M. A.; Li, C.; Chen, W. Copper Sulfide Nanoparticles for Photothermal Aablation of Tumor Cells. *Nanomedicine* **2010**, *5*, 1161−1171.
(17) Hessel, C. M.; Pattani, V. P.; Rasch, M.; Panthani, M. G.; Koo, B.; Tunnell, J. W.; Korgel, B. A. Copper Selenide Nanocrystals for Photothermal Therapy. *Nano Lett.* **2011**, *11*, 2560−2566.
(18) Hsu, S. W.; On, K.; Tao, A. R. Localized Surface Plasmon Resonances of Anisotropic Semiconductor Nanocrystals. *J. Am. Chem. Soc.* **2011**, *133*, 19072−19075.
(19) Mansour, B. A.; Farag, B. S.; Khodier, S. A. Transport-Properties and Band-Structure of Nonstoichiometric $Cu_{2-x}Te$. *Thin Solid Films* **1994**, *247*, 112−119.
(20) Loferski, J. J. Theoretical Considerations Governing the Choice of the Optimum Semiconductor for Photovoltaic Solar Energy Conversion. *J. Appl. Phys.* **1956**, *27*, 777−784.
(21) Zhou, J.; Wu, X.; Duda, A.; Teeter, G.; Demtsu, S. H. The Formation of Different Phases of Cu_xTe and Their Effects on CdTe/CdS Solar Cells. *Thin Solid Films* **2007**, *515*, 7364−7369.
(22) Pashinkin, A. S.; Fedorov, V. A. Phase Equilibria in the Cu−Te System. *Inorg. Mater.* **2003**, *39*, 539−554.
(23) Li, B.; Xie, Y.; Huang, J. X.; Su, H. L.; Qian, Y. T. A Solvothermal Route to Nanocrystalline Cu_7Te_4 at Low Temperature. *J. Solid State Chem.* **1999**, *146*, 47−50.
(24) Kumar, P.; Singh, K. Element Directed Aqueous Solution Synthesis of Copper Telluride Nanoparticles, Characterization, and Optical Properties. *Cryst. Growth Des.* **2009**, *9*, 3089−3094.
(25) Li, B.; Xie, Y.; Huang, J. X.; Liu, Y.; Qian, Y. T. Sonochemical Synthesis of Nanocrystalline Copper Tellurides Cu_7Te_4 and Cu_4Te_3 at Room Temperature. *Chem. Mater.* **2000**, *12*, 2614−2616.
(26) Yang, J.; Yu, S. H.; Han, Z. H.; Qian, Y. T.; Zhang, Y. H. Synthesis and Phase Transformation of IB-VIA Nonstoichiometric Nanocrystalline Tellurides by a Hydrothermal-Reduction Process. *J. Solid State Chem.* **1999**, *146*, 387−389.
(27) She, G. W.; Zhang, X. H.; Shi, W. S.; Cai, Y.; Wang, N.; Liu, P.; Chen, D. M. Template-Free Electrochemical Synthesis of Single-Crystal CuTe Nanoribbons. *Cryst. Growth Des.* **2008**, *8*, 1789−1791.
(28) Aliyev, Y. I.; Asadov, Y. G.; Babaev, A. G.; Jafarov, K. M.; Mageramova, F. G.; Aliyeva, R. D. Polymorphic Transformation of $Cu_{1.80}Te$ Crystals. *Inorg. Mater.* **2011**, *47*, 356−360.
(29) Zhang, L. Z.; Ai, Z. H.; Jia, F. L.; Liu, L.; Hu, X. L.; Yu, J. C. Controlled Hydrothermal Synthesis and Growth Mechanism of Various Nanostructured Films of Copper and Silver Tellurides. *Chem.—Eur. J.* **2006**, *12*, 4185−4190.
(30) Zhang, Y.; Qiao, Z. P.; Chen, X. M. Microwave-Assisted Elemental Direct Reaction Route to Nanocrystalline Copper Chalcogenides CuSe and Cu_2Te. *J. Mater. Chem.* **2002**, *12*, 2747−2748.
(31) Zhang, Y.; Ni, Y.; Wang, X.; Xia, J.; Hong, J. Polycrystalline Cu_7Te_4 Dendritic Microstructures Constructed by Spherical Nanoparticles: Fast Electrodeposition, Influencing Factors, and the Shape Evolution. *Cryst. Growth Des.* **2011**, *11*, 4368−4377.
(32) Kriegel, I.; Jiang, C. Y.; Rodriguez-Fernandez, J.; Schaller, R. D.; Talapin, D. V.; Da Como, E.; Feldmann, J. Tuning the Excitonic and Plasmonic Properties of Copper Chalcogenide Nanocrystals. *J. Am. Chem. Soc.* **2012**, *134*, 1583−1590.
(33) Shen, H. B.; Jiang, X. D.; Wang, S. J.; Fu, Y. T.; Zhou, C. H.; Li, L. S. Facile Preparation of Metal Telluride Nanocrystals Using Di-n-octylphosphine Oxide (DOPO) as an Air-Stable and Less Toxic Alternative to the Common Tri-alkylphosphines. *J. Mater. Chem.* **2012**, *22*, 25050−25056.
(34) Xiao, G. J.; Zeng, Y.; Jiang, Y. Y.; Ning, J. J.; Zheng, W. T.; Liu, B. B.; Chen, X. D.; Zou, G. T.; Zou, B. Controlled Synthesis of Hollow $Cu_{2-x}Te$ Nanocrystals Based on the Kirkendall Effect and Their Enhanced CO Gas-Sensing Properties. *Small* **2013**, *9*, 793−799.
(35) Kriegel, I.; Rodríguez-Fernández, J.; Wisnet, A.; Zhang, H.; Waurisch, C.; Eychmuller, A.; Dubavik, A.; Govorov, A. O.; Feldmann, J. Shedding Light on Vacancy-Doped Copper Chalcogenides: Shape-Controlled Synthesis, Optical Properties, and Modeling of Copper Telluride Nanocrystals with Near-Infrared Plasmon Resonances. *ACS Nano* **2013**, *7*, 4367−4377.
(36) Henzie, J.; Lee, J.; Lee, M. H.; Hasan, W.; Odom, T. W. Nanofabrication of Plasmonic Structures. *Annu. Rev. Phys. Chem.* **2009**, *60*, 147−165.
(37) Templeton, A. C.; Pietron, J. J.; Murray, R. W.; Mulvaney, P. Solvent Refractive Index and Core Charge Influences on the Surface Plasmon Absorbance of Alkanethiolate Monolayer-Protected Gold Clusters. *J. Phys. Chem. B* **2000**, *104*, 564−570.
(38) Yin, Y. D.; Erdonmez, C. K.; Cabot, A.; Hughes, S.; Alivisatos, A. P. Colloidal Synthesis of Hollow Cobalt Sulfide Nanocrystals. *Adv. Funct. Mater.* **2006**, *16*, 1389−1399.
(39) Yin, Y. D.; Rioux, R. M.; Erdonmez, C. K.; Hughes, S.; Somorjai, G. A.; Alivisatos, A. P. Formation of Hollow Nanocrystals Through the Nanoscale Kirkendall Effect. *Science* **2004**, *304*, 711−714.
(40) Aldinger, F. Controlled Porosity by an Extreme Kirkendall Effect. *Acta Metall.* **1974**, *22*, 923−928.
(41) Fan, H. J.; Scholz, R.; Kolb, F. M.; Zacharias, M.; Gosele, U. Growth Mechanism and Characterization of Zinc Oxide Microcages. *Solid State Commun.* **2004**, *130*, 517−521.
(42) Sorokin, G. P.; Papshev, Y. M.; Oush, P. T. Photoconductivity of Cu_2S, Cu_2Se, and Cu_2Te. *Sov. Phys. Solid State* **1966**, *7*, 1810−1811.
(43) Farag, B. S.; Khodier, S. A. Direct and Indirect Transitions in Copper Telluride Thin-Films. *Thin Solid Films* **1991**, *201*, 231−240.
(44) Zhao, Y. X.; Burda, C. Development of Plasmonic Semiconductor Nanomaterials with Copper Chalcogenides for a Future with Sustainable Energy Materials. *Energy Environ. Sci.* **2012**, *5*, 5564−5576.
(45) Gao, F. F.; Cheng, Y. M.; Yu, Q. J.; Liu, S.; Shi, D.; Li, Y. H.; Wang, P. Conjugation of Selenophene with Bipyridine for a High Molar Extinction Coefficient Sensitizer in Dye-Sensitized Solar Cells. *Inorg. Chem.* **2009**, *48*, 2664−2669.
(46) Cademartiri, L.; Montanari, E.; Calestani, G.; Migliori, A.; Guagliardi, A.; Ozin, G. A. Size-Dependent Extinction Coefficients of PbS Quantum Dots. *J. Am. Chem. Soc.* **2006**, *128*, 10337−10346.
(47) Dai, Q. Q.; Wang, Y. N.; Li, X. B.; Zhang, Y.; Pellegrino, D. J.; Zhao, M. X.; Zou, B.; Seo, J.; Wang, Y. D.; Yu, W. W. Size-Dependent

Composition and Molar Extinction Coefficient of PbSe Semiconductor Nanocrystals. *ACS Nano* **2009**, *3*, 1518−1524.
(48) Liu, X. O.; Atwater, M.; Wang, J. H.; Huo, Q. Extinction Coefficient of Gold Nanoparticles with Different Sizes and Different Capping Ligands. *Colloids Surf., B* **2007**, *58*, 3−7.
(49) Liao, H. W.; Hafner, J. H. Gold Nanorod Bioconjugates. *Chem. Mater.* **2005**, *17*, 4636−4641.
(50) Schwartzberg, A. M.; Olson, T. Y.; Talley, C. E.; Zhang, J. Z. Synthesis, Characterization, and Tunable Optical Properties of Hollow Gold Nanospheres. *J. Phys. Chem. B* **2006**, *110*, 19935−19944.
(51) Teperik, T. V.; Popov, V. V.; García de Abajo, F. J. Radiative Decay of Plasmons in a Metallic Nanoshell. *Phys. Rev. B* **2004**, *69*, 155402.
(52) Hao, E.; Li, S.; Bailey, R. C.; Zou, S.; Schatz, G. C.; Hupp, J. T. Optical Properties of Metal Nanoshells. *J. Phys. Chem. B* **2004**, *108*, 1224−1229.
(53) Malinsky, M. D.; Kelly, K. L.; Schatz, G. C.; Van Duyne, R. P. Nanosphere Lithography: Effect of Substrate on the Localized Surface Plasmon Resonance Spectrum of Silver Nanoparticles. *J. Phys. Chem. B* **2001**, *105*, 2343−2350.
(54) Farag, B. S.; Khodier, S. A. Spectral Dependence of the Absorption-Coefficient of Thin-Films of Nonstoichiometric $Cu_{2-x}Te$. *Thin Solid Films* **1991**, *205*, 52−57.
(55) Riha, S. C.; Johnson, D. C.; Prieto, A. L. Cu_2Se Nanoparticles with Tunable Electronic Properties Due to a Controlled Solid-State Phase Transition Driven by Copper Oxidation and Cationic Conduction. *J. Am. Chem. Soc.* **2011**, *133*, 1383−1390.
(56) Miyatani, S. Y.; Mori, S.; Yanagihara, M. Phase-Diagram and Electrical-Properties of Cu_2-Delta-Te. *J. Phys. Soc. Jpn.* **1979**, *47*, 1152−1158.
(57) Miller, M. M.; Lazarides, A. A. Sensitivity of Metal Nanoparticle Surface Plasmon Resonance to the Dielectric Environment. *J. Phys. Chem. B* **2005**, *109*, 21556−21565.
(58) Shi Kam, N. W.; O'Connell, M.; Wisdom, J. A.; Dai, H. Carbon Nanotubes as Multifunctional Biological Transporters and Near-Infrared Agents for Selective Cancer Cell Destruction. *Proc. Natl. Acad. Sci. U.S.A.* **2005**, *102*, 11600−11605.